https://doi.org/10.15407/ujpe71.2.173

N. GOMIDZE, D. JAKOBIA, M. KHAJIDHVILI, L. KALANDADZE, I. JABNIDZE, K. MAKHARADZE, O. NAKASHIDZE, J. SHAINIDZE

Department of Physics, Batumi Shota Rustaveli State University
(35, Ninoshvili Str., Batumi, Georgia; e-mail: gomidze@bsu.edu.ge)

LASER-INDUCED BREAKDOWN SPECTROSCOPY PLASMAS AS A TESTBED FOR NON-EQUILIBRIUM PLASMA MODELING IN HIGH-ENERGY PHYSICS APPLICATIONS[1]

Laser-induced breakdown spectroscopy (LIBS) enables rapid elemental analysis and plasma diagnostics but suffers from limited quantitative accuracy due to the strong spatiotemporal nonuniformity of the laser-induced plasma and stochastic fluctuations in ionization-recombination kinetics. In this work, we develop and experimentally validate a deterministic–stochastic framework that couples classical rate equations with stochastic differential terms to capture shot-to-shot plasma variability. The model, implemented through a first-order Runge–Kutta (RK1) scheme augmented by the Euler–Maruyama method, is quantitatively related to standard LIBS diagnostics: Stark broadening for electron density (n_e), the LTE Saha equation for ionization balance, and Boltzmann plots for excitation temperature ($T_{\rm exc}$). Single-shot LIBS experiments using a 1064 nm, 7 ns Nd : YAG laser were performed on six metals (Al, Cu, brass, Pb, stainless steel, and Ti) under identical conditions. The measured spectra showed high reproducibility (intensity scatter <7%), and the extracted plasma parameters revealed consistent material-dependent trends: Al and stainless steel exhibited the highest n_e (up to (7–9) $\times 10^{18}$ cm^{-3}), whereas Cu and brass showed lower values ($\sim$(2–3) $\times 10^{18}$ cm^{-3}). Electron temperatures derived from the Saha equation reached 12–13 kK for high-ionization materials and <11 kK for low-ionization ones. The introduction of a stochastic fluctuation term ($\sigma \approx 0.05$) reproduced the observed intensity scatter and improved agreement between modeled and experimental spectra. The proposed framework enhances LIBS diagnostic accuracy under transient, non-equilibrium conditions and provides a compact laboratory analogue for studying fluctuation-driven plasma dynamics relevant to high-energy-density physics, laser–plasma interactions, and fusion environments. This unified deterministic–stochastic treatment bridges applied laser spectroscopy with the broader physics of non-LTE plasmas.

Keywords: laser-induced plasma (LIP), Saha equation, Boltzmann plot, stochastic modeling, high-energy density physics, non-LTE plasma.

1. Introduction

Laser-induced plasmas (LIP) are produced when a high-energy laser pulse ablates the surface of a condensed material, creating a rapidly expanding plasma plume with strong gradients of temperature, electron density, and degree of ionization. Such short-lived

[1] This work is based on the results presented at the 2025 "New Trends in High-Energy Physics" Conference.

Citation: Gomidze N., Jakobia D., Khajidhvili M., Kalandadze L., Jabnidze I., Makharadze K., Nakashidze O., Shainidze J. Laser-induced breakdown spectroscopy plasmas as a testbed for non-equilibrium plasma modeling in high-energy physics applications. *Ukr. J. Phys.* **71**, No. 2, 173 (2026). https://doi.org/10.15407/ujpe71.2.173.

nonequilibrium systems not only underpin applied techniques such as laser-induced breakdown spectroscopy (LIBS), pulsed laser deposition, and laser welding, but also represent microscale analogues of high-energy plasmas encountered in fusion, astrophysical, and accelerator environments. The dynamics of energy transfer, ionization, and recombination in these systems resemble those observed in large-scale laser–plasma interactions and in relativistic particle–beam experiments [1–3, 14–17].

The quantitative interpretation of LIBS spectra is limited by the spatiotemporal non-uniformity of the plasma and by stochastic fluctuations in the evolution of its microscopic parameters. Deterministic models of plasma kinetics are often insufficient to describe the observed shot-to-shot variability, which originates from random perturbations of electron density, temperature, and local electric fields. These fluctuations are conceptually similar to turbulence and stochastic energy exchange processes studied in high-energy density physics, where ionization and recombination occur under rapidly changing, non-local thermodynamic equilibrium (non-LTE) conditions [3, 12–13].

Accurate spectroscopic diagnostics therefore require combined deterministic–stochastic approaches capable of capturing both the mean-field evolution and its fluctuations. Among classical diagnostic tools, Boltzmann plots and Stark broadening are routinely employed to estimate the excitation temperature and electron density [4–5], while the Saha equation and radiative transfer models provide a baseline for ionization balance [6]. However, under transient conditions typical of LIP, these methods must be supplemented by stochastic kinetic modeling to reproduce observed plasma behavior.

Recent developments in two-fluid and magnetohydrodynamic (MHD) descriptions have further emphasized the need to treat electrons and ions as dynamically distinct species. Such models predict electrostatic Langmuir oscillations and, under magnetized conditions, Alfvén-type modes that govern plasma transport and wave–particle interactions [14–17]. These same processes are fundamental to the physics of high-energy plasmas in fusion devices, astrophysical jets, and wakefield accelerators. Consequently, LIBS plasmas – although small in scale – offer a controlled laboratory platform for investigating fluctuation-driven plasma instabilities relevant to those extreme environments.

Building upon our previous works on the statistical moments of laser scattering through random phase screens [7] and the numerical analysis of fluorescence in aqueous media [9–10], we apply a similar stochastic formalism to LIBS plasma emission. The present study develops a deterministic–stochastic framework for ionization–recombination kinetics, combining first-order Runge–Kutta integration with stochastic differential equations solved via the Euler–Maruyama scheme [18]. This approach connects classical LIBS diagnostics (Boltzmann plots, Stark broadening, and the Saha relation) with modern kinetic theories used in high-energy plasma modeling, thereby bridging analytical laser spectroscopy and the broader domain of high-energy and nonequilibrium plasma physics.

2. Problem Statement

Laser-induced breakdown spectroscopy (LIBS) is a powerful technique for elemental and plasma diagnostics, yet, its quantitative accuracy is fundamentally constrained by the spatiotemporal non-uniformity of the laser-induced plasma. In practice, rapid fluctuations of the electron temperature (T_e) and electron density (n_e) distort spectral line shapes and intensities through Stark broadening and self-absorption (opacity), thereby complicating spectral inversion and calibration [1–2].

Moreover, shot-to-shot and intra-shot variations in ionization–recombination kinetics cause measurable scatter in emitted line intensities, reflecting the inherently stochastic nature of plasma evolution. Such variability cannot be adequately captured by purely deterministic rate equations.

Traditional equilibrium approaches, including the local thermodynamic equilibrium (LTE) Saha equation, fail to describe non-LTE conditions typical of transient laser plasmas, where steep temperature gradients and radiative processes dominate. These non-equilibrium regimes require models that simultaneously account for deterministic transport and stochastic fluctuations in microscopic plasma parameters.

Therefore, the objectives of this study are to:

• develop a modeling framework that couples deterministic ionization–recombination kinetics with a stochastic extension to capture the experimentally observed variability in LIBS plasmas.

• Validate the framework experimentally using high-resolution LIBS spectra acquired under controlled laboratory conditions.

• Establish a consistent diagnostic workflow integrating Boltzmann plots (for T_e), Stark broadening (for n_e), and intensity-ratio checks to minimize uncertainty in inferred plasma parameters.

This approach not only enhances the reliability of LIBS diagnostics but also contributes to the broader understanding of fluctuation-driven processes in non-equilibrium plasmas – an issue central to both laser – matter interaction physics and high-energy density plasma research.

3. Theoretical Background and Computational Modeling

When analyzing the early-stage dynamics of laser-induced plasma (LIP), it is necessary to treat electrons and ions as two distinct interacting fluids. Unlike the single-fluid magnetohydrodynamic (MHD) approximation, which assumes that all charged species move collectively, the two-fluid approach separates the dynamics of electrons and ions, allowing their different inertia and response times to be properly captured. In this framework, the governing equations include both mass conservation and momentum balance for each species.

The continuity equations for electrons and ions are

$$\frac{\partial n_s}{\partial t} + \nabla \cdot (n_s \mathbf{v}_s) = 0 \quad (s = e, i) \tag{1}$$

while the momentum balance equations take the form:

$$lm_s n_s \left(\frac{\partial \mathbf{v}_s}{\partial t} + \mathbf{v}_s \cdot \nabla \mathbf{v}_s \right) =$$

$$= -\nabla p_s + q_s n_s (\mathbf{E} + [\mathbf{v}_s \times \mathbf{B}]) - \mathbf{R}_{ei}, \tag{2}$$

where n_s, m_s, and $\mathbf{v}_s$ are the density, mass, and velocity of species s, respectively; p_s is the partial pressure, and $\mathbf{R}_{ei} = m_e n_e \nu_{ei} (\mathbf{v}_e - \mathbf{v}_i)$ is the electron–ion momentum exchange term due to collisions. This formulation ensures that both mass conservation and collisional coupling are explicitly included, avoiding the inconsistency of neglecting collisions in the steady-state limit. Such a description is particularly relevant to LIBS plasmas, where strong electron–ion interactions during the first tens of nanoseconds determine the evolution of density perturbations, spectral line broadening, and the effective ionization–recombination balance observed in emission spectra. Because the electron mass is very small, its inertia can be neglected on time scales longer than the electron plasma period. Under these conditions, the electron momentum equation reduces to a fast balance between the pressure gradient, the electric field, and the magnetic (Lorentz) force:

$$0 = -\nabla p_e - n_\mathrm{e}(\mathbf{E} + [\mathbf{v}_\mathrm{e} \times \mathbf{B}]), \tag{3}$$

where the collisional drag term is small but not strictly zero and is retained as a perturbation when necessary.

This approximation is justified for LIBS plasmas, where electrons respond almost instantaneously, while the heavy ions remain quasi-stationary over the nanosecond timescale.

If ions are assumed immobile ($v_i = 0$), the plasma supports electrostatic oscillations (Langmuir waves) in which electrons oscillate against a stationary ion background. The perturbed quantities are expressed as:

$$n = n_0 + \delta n_e, \quad \mathbf{v}_e = \delta \mathbf{v}_e, \quad \mathbf{E} = \delta \mathbf{E}. \tag{4}$$

The linearized electron momentum equation is then:

$$m_\mathrm{e} \frac{\partial \delta \mathbf{v}_\mathrm{e}}{\partial t} = -e\delta \mathbf{E} - \frac{\nabla p_\mathrm{e}}{n_0}, \tag{5}$$

where pressure perturbations are related to density perturbations by:

$$\frac{\partial \delta n_e}{\partial t} + n_0 \nabla \cdot (\delta \mathbf{v}_e) = 0. \tag{6}$$

For high-frequency Langmuir oscillations, electrons behave adiabatically with an effective adiabatic index $\gamma_e \approx 3$, corresponding to the well-known Bohm–Gross correction factor. The electron continuity equation becomes:

$$\frac{\partial \delta n_e}{\partial t} + n_0 \nabla \cdot (\delta \mathbf{v}_e) = 0. \tag{7}$$

The electron continuity equation is supplemented by Gauss's law:

$$\nabla \cdot \delta \mathbf{E} = \frac{e\, \delta n_e}{\varepsilon_0}. \tag{8}$$

Combining Eqs. (5)–(8) yields the dispersion relation for electrostatic electron–plasma oscillations:

$$\omega^2 = \omega_L^2 + 3k^2 v_{te}^2, \tag{9}$$

where $v_{th,e} = \sqrt{k_\mathrm{B} T_e / m_e}$ – is the electron thermal velocity and $\omega_L = \sqrt{n_0 e^2/(\varepsilon_0 m_\mathrm{e})}$ is the frequency of the electron plasma – the Langmuir frequency. Equation (9) represents the Bohm–Gross dispersion for Langmuir-type oscillations. If a magnetic field is present and ion inertia is included, Alfvén-type modes appear with

$$\omega^2 \approx k_\parallel^2 v_A^2, \quad v_A = B/\sqrt{\mu_0 \mu_i m_i},$$

but under weakly magnetized, short-pulse LIBS conditions, the electrostatic (Langmuir) term dominates. These local density–field oscillations modulate microscopic electric fields and hence influence Stark broadening and line-shape asymmetry, directly linking the two-fluid analysis to experimental diagnostics. For completeness, Alfvén waves arise only when magnetic tension and ion inertia are retained in the full MHD/two-fluid formulation; their characteristic times are orders of magnitude longer than the nanosecond electrostatic oscillations considered here. Consequently, the Langmuir-mode microfield fluctuations derived above are the physically relevant mechanism behind the observed Stark line broadening in our LIBS setup.

3.1. Ionization–recombination modeling

In laser-induced plasmas, evaluating the degree of ionization is crucial for quantitative analysis. Under equilibrium conditions, the ionization process is governed by the Saha equation, derived from statistical mechanics by equalizing the chemical potentials of neutral atoms, ions, and electrons:

$$\mu_i = \mu_{i+1} + \mu_e, \ \mu = k_\mathrm{B} T \ln\left(\frac{ng}{z}\right), \tag{10}$$

where n is the particle concentration, g is the statistical weight, and Z is the partition function. Combining these expressions yields the canonical form of the Saha equation:

$$\frac{n_{\mathrm{i}+1} n_\mathrm{e}}{n_\mathrm{i}} = \frac{2}{\Lambda^3} \frac{Z_{\mathrm{i}+1}(T)}{Z_\mathrm{i}(T)} \exp\left(-\frac{E_{\mathrm{ion},\,i}}{k_\mathrm{B} T}\right). \tag{11}$$

Where

$$\Lambda_T = \left(\frac{h^2}{2\pi m_e k_\mathrm{B} T}\right)^{1/2}$$

is the electron thermal de Broglie wavelength, $E_{\mathrm{ion},\,i}$ is the ionization energy, and the factor 2 accounts for electron spin degeneracy. Equation (11) defines an LTE (local thermodynamic equilibrium) baseline for ionization balance.

In practice, LIBS plasmas frequently deviate from LTE because collisional processes alone cannot maintain equilibrium during the early nanoseconds after ablation. In such non-LTE regimes, radiative transitions become comparable to collisional ones, and the full collisional–radiative (CR) model must be employed:

$$\frac{dn_i}{dt} = n_\mathrm{e}\left[n_{\mathrm{i}-1}\, S_{i-1}^{\mathrm{ion}}(T_\mathrm{e}) - n_\mathrm{i}\, \alpha_i^{\mathrm{rec}}(T_\mathrm{e})\right], \tag{12}$$

where S^{ion} and α^{rec} are the ionization and recombination rate coefficients. The plasma quasi-neutrality condition requires:

$$n_\mathrm{e} = \sum_{j=1}^{Z_{\max}} (j n_j), \quad n_{\mathrm{tot}} = \sum_{j=1}^{Z_{\max}} (n_j). \tag{13}$$

A practical diagnostic employs the intensity ratio of ionized to neutral emission lines:

$$\frac{I_{\mathrm{ion}}}{I_{\mathrm{neutral}}} \longrightarrow \mathcal{C} \cdot \frac{n_{i+1}}{n_i}, \tag{14}$$

where $\mathcal{C}$ depends on the transition probability A_{ki}, wavelength λ, and other spectroscopic constants (from NIST [23]). This relation allows indirect estimation of the plasma's ionization degree and, via Eq. (11), its electron temperature T_e, provided that lines are optically thin and belong to the same element.

After laser ablation, the plasma contains neutral atoms (A), free electrons (e^-), singly ionized ions (A^+), and doubly ionized ions (A^{2+}). For typical LIBS conditions ($T_e \approx 1.5 \times 10^4$ K, $n_{\mathrm{tot}} \approx \approx 10^{18}$ cm^{-3}), the populations of these species evolve dynamically under competing ionization and recombination processes.

Because each ionization stage contributes a different number of free electrons:

$$n_\mathrm{e} = n_1 + 2 \cdot n_2 + 3 \cdot n_3, \tag{15}$$

while the total atomic concentration is:

$$\eta_{\mathrm{total}} = \eta_0 + \eta_1 + \eta_2 + \eta_3. \tag{16}$$

3.2. Stochastic extension

To represent experimentally observed variability in line intensities and ion populations, a stochastic term is added to the rate equations:

$$n_i(t+\Delta t) = n_i(t) + \Delta t \cdot \frac{dn_i}{dt} + \epsilon_i(t), \tag{17}$$

where $\epsilon_i(t) \sim N(0, \sigma_i^2)$ describes random deviations caused by microscopic ion–electron collisions. An additive noise model was adopted with a typical fluctuation amplitude $\sigma \approx 0.05$, consistent with the observed relative standard deviation ($RSD \approx 4$–6%) of spectral line intensities in replicate LIBS shots [4, 13]. Time-step sensitivity tests (halving Δt) produced <2% variation in mean populations, confirming numerical stability. This stochastic extension effectively captures shot-to-shot plasma variability and provides confidence intervals for predicted level populations and line intensities. Together with the deterministic framework, it forms the theoretical basis for the diagnostic workflow presented in Section 4.

3.3. Relation to high-energy plasma physics

The two-fluid and stochastic analyses outlined above are not limited to LIBS applications. They parallel the theoretical treatments of high-energy-density plasmas, where rapid ionization, wave-particle interactions, and fluctuation-driven instabilities govern plasma behavior. The derived Bohm–Gross dispersion mirrors the oscillations observed in laser-plasma wakefield accelerators and fusion plasmas, while the inclusion of stochastic kinetics resembles modeling approaches used in non-LTE radiative transport and dense plasma recombination studies [14–17]. Thus, LIBS provides a compact laboratory analogue of the fundamental processes explored in modern high-energy plasma physics.

4. Objectives and Research Methodology

4.1. Objectives

We aim to (i) acquire reproducible single-shot LIBS spectra from six metals under controlled conditions, (ii) extract plasma parameters (T_e, n_e) from line shapes and intensities, and (iii) benchmark these measurements against the deterministic–stochastic modeling of ionization–recombination dynamics (Section 3).

Fig. 1. StellarNet Blue-Wave (200–400 nm) spectroscopic system for LIBS and absorption measurements: laser–target interaction, optical fiber collection, and spectrometer-based detection

4.2. Experimental setup and samples

The experimental setup employed a StellarNet Blue-Wave UV spectrometer operating in the 200–400 nm range with an average spectral resolution of about 1 nm. This range encompasses the most prominent neutral and ionized emission lines (Al I 394.4 nm, Al II 358.7 nm, Cu I 324.7 nm, Fe I 302.1 nm, Ti I 368.5 nm, *etc.*), providing optimal conditions for plasma diagnostics in the ultraviolet region. The spectrometer was coupled via a 600 μm fiber to the observation optics at 45°, while the plasma was generated by a Q-switched Nd : YAG laser (1064 nm, 7 ns) focused through a 100 mm plano-convex lens. The system configuration allows both emission (LIBS) and absorption modes to be recorded without realignment, ensuring consistent geometry and reproducible results (Fig. 1).

• Laser & optics. Q-switched Nd : YAG ($\lambda = 1064$ nm, $\tau \approx 7$ ns, 1 Hz); focusing with a 100 mm plano-convex lens normal to the target. Spot size $\sim 100\,\mu$m verified by the knife-edge method; at 70 mJ the fluence is ~ 89 J cm^{-2}.

• Collection & detection. Emission collected at 45° with a 600 μm fiber and dispersed by a StellarNet BlackComet-SR (200–1100 nm, instrumental

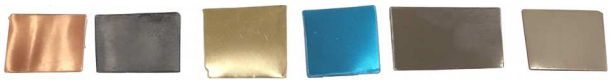

Fig. 2. Approximately equal-size samples selected for analysis

FWHM ∼1.5 nm). Spectra are single-shot integrated (no gating).

• Samples. Cu, brass (Cu–Zn), Pb, Al, stainless steel (Fe–Cr–Ni), Ti; thickness 0.1–0.5 mm (Fig. 2). Surfaces were cleaned immediately before ablation to minimize oxides/contamination. Targets were clamped on a black ceramic mount; thin foils (0.1 mm Cu, brass) on a sacrificial ceramic backing to prevent perforation. Shots were laterally separated by ≥0.2–0.5 mm to avoid crater overlap.

• Ambient. Air, ∼1 atm. In the selected lines, Stark broadening dominates over pressure broadening at our resolution.

For metals at 1064 nm the optical skin depth δ is typically tens of nm and scales as $\delta \approx \sqrt{2/(\mu_0 \sigma \omega)}$; hence δ sets the initial energy-deposition volume and, together with thermal transport, influences early-time plasma conditions.

4.3. Calibration and acquisition protocol

Low-pressure Hg(Ar) lamp before/after runs; drift <0.05 nm. Instrumental FWHM ∼1.5 nm used as the Gaussian constraint in Voigt fits. For each material, three independent single shots under identical settings. Baseline correction; peak finding; intensities normalized across triplicates to reduce cross-sample variability.

4.4. Line assignment and data-analysis workflow

• Peaks matched to NIST ASD (air wavelengths) within ±(0.2–0.3) nm;

• levels (E_u, E_l), A_{ul}, multiplet companions cross-checked. Strongly self-absorbed or blended lines were excluded or deconvolved.

• Voigt fits with instrumental Gaussian width fixed ($\Delta\lambda_G^2 = \Delta\lambda_{\text{inst}}^2 + \Delta\lambda_D^2$; here $\Delta\lambda_D < \Delta\lambda_{\text{inst}}$). The Lorentzian component is taken as $\Delta\lambda_{1/2}^{\text{Stark}}$. When fits were unstable, the quadratic subtraction $\Delta\lambda_{\text{Stark}} \approx \sqrt{\Delta\lambda_{\text{meas}}^2 - \Delta\lambda_{\text{inst}}^2}$ was used as an approximation. Electron density from tabulated ω (nm per 10^{16} cm^{-3}):

$$\nabla\lambda_{1/2}^{\text{Stark}} \approx 2\omega \left(\frac{n_e}{10^{16}\,\text{cm}^{-3}}\right) \rightarrow n_e = \frac{\Delta\lambda_{1/2}^{\text{Stark}}}{2\omega} \times 10^{16}\,\text{cm}^{-3}.$$

• 3–6 unblended lines of the same element and charge state; $y = \ln(I\lambda/(g_u A_{ul}))$ vs $x = E_u$; slope $= -1/(k_B T)$. Only fits with $R^2 \geq 0.95$ reported. In single-shot integrated spectra T_{exc} is an effective excitation temperature and may differ from T_e.

• For optically thin lines: $I_{\text{ion}}/I_{\text{neutral}} = \mathcal{C}\,(n_{i+1}/n_i)$, with $\mathcal{C}$ reflecting $\lambda, A_{ul}, g_u, Z(T)$. It is used as an LTE baseline (Saha) at the measured n_e; non-LTE absolute populations require a CR model.

The laser energy and other parameters were fixed, which significantly increased the importance of surface preparation and sample mounting. Several laser pulses were applied to each sample, and the resulting spectra were recorded in different wavelength ranges (189–410 nm). For each material, characteristic neutral and ionized lines were selected, as presented in Table 1.

Using the LTE Saha relation (Eq. 11) together with the measured intensity ratio $I_{\text{ion}}/I_{\text{neutral}}$ (Eq. 14), the averages in Table 1 serve as a baseline indicator for the ionization balance n_{i+1}/n_i at the measured n_e. Higher ratios (e.g., Al, Cu, brass) indicate larger n_{i+1}/n_i and correspond to higher T_e; lower ratios (Pb, Ti, stainless steel) indicate smaller n_{i+1}/n_i and lower T_e, other conditions being similar. These trends are consistent with the Stark-derived n_e and the use of lines with minimal self-absorption. We emphasize that this inference relies on LTE and is intended to capture trends; absolute values under non-LTE conditions would require a collisional–radiative analysis (Table 2).

For each spectrum, characteristic emission lines were identified; the wavelength of each peak maximum was read with ±0.1 nm precision (from prior calibration), and the intensity (a.u.) was taken as the peak height after local baseline subtraction. To compare materials, intensities were normalized to the mean of the three replicates per target, which reduces variability due to minor surface/thickness differences. (FWHM extraction and instrumental-broadening correction are applied later in the Stark analysis section.)

For copper, three single-shot spectra acquired under the same conditions (Fig. 3) show strong reproducibility. The most intense lines at 324.7 nm and 327.4 nm (Cu I) are consistently present; residual in-

Table 1. **Identification of neutral (I) and ionized (II) emission lines and average ionization ratios ($I_{\text{ion}}/I_{\text{neutral}}$) for analyzed materials**

Material (sample)	Neutral line (nm)	Ionized line (nm)	Average ratio $I_{\text{ion}}/I_{\text{neutral}}$
Copper (Cu)	324.7 (Cu I)	213.6 (Cu II)	0.35–0.40
Brass (Cu+Zn)	324.7 (Cu I)	213.6 (Cu II) (+ Zn II 334.5)	0.38–0.42
Lead (Pb)	367.1 (Pb I)	220.4 (Pb II)	0.30–0.35
Aluminium (Al)	394.4, 396.1 (Al I)	358.7 (Al II)	0.40–0.50
Stainless Steel (Fe–Cr–Ni)	302.1 (Fe I)	259.9 (Fe II)	0.25–0.30
Titanium (Ti)	368.5 (Ti I)	337.3 (Ti II)	0.30–0.35

Table 2. **Neutral lines: FWHM and n_e (from Stark broadening)**

Material	Neutral line (nm)	FWHM (nm)	Stark const. ω (nm/10^{16} cm^{-3})	n_e (10^{18} cm^{-3})
Aluminium	394.4	1.75	0.0012	7.29
Copper	324.7	0.75	0.0011	3.41
Brass (Cu+Zn)	324.7	0.50	0.0011	2.27
Lead	367.1	Insufficient SNR	0.0013	Insufficient SNR
Stainless steel	302.1	1.75	0.0010	8.75
Titanium	368.5	0.50	0.0012	2.08

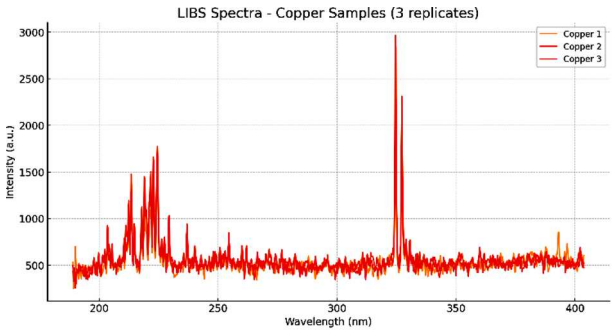

Fig. 3. Spectral profiles of the three replicates of copper

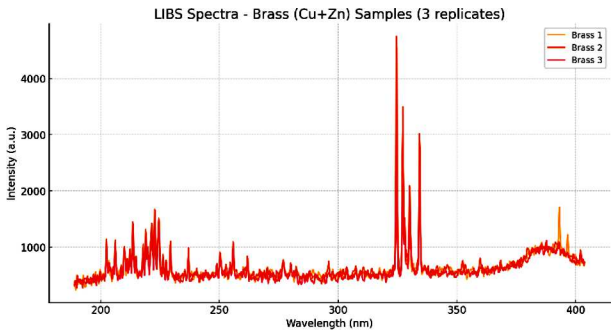

Fig. 4. Spectral profiles of the three replicates of brass

tensity scatter <5% is attributed to surface roughness and small variations in the ablation spot position.

Brass (Cu–Zn): Under identical conditions, three single-shot spectra of brass were recorded; the overlaid profiles are shown in Fig. 4. The spectra are highly reproducible and exhibit the expected Cu I lines at 324.7 and 327.4 nm, together with Zn I lines at 213.9, 334.5, and 468.0 nm. Shot-to-shot intensity scatter is <7%, attributable to small differences in ablation spot location and surface microstructure.

Lead (Pb): Under identical conditions, three single-shot spectra of lead were recorded; the overlaid

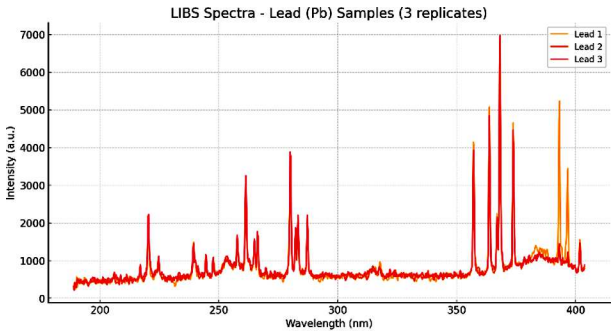

Fig. 5. Spectral profiles of the three replicates of lead

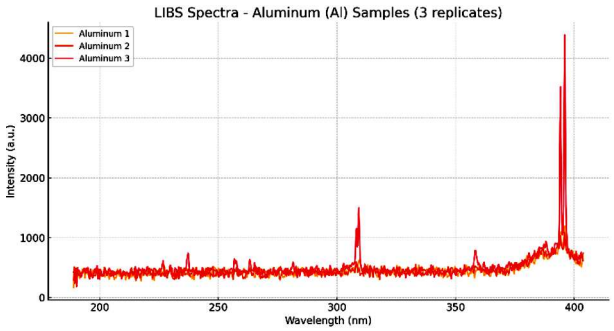

Fig. 6. Spectral profiles of the three replicates of aluminium

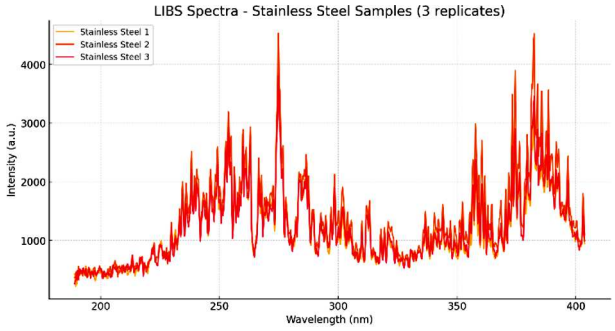

Fig. 7. Spectral profiles of the three replicates of stainless steel

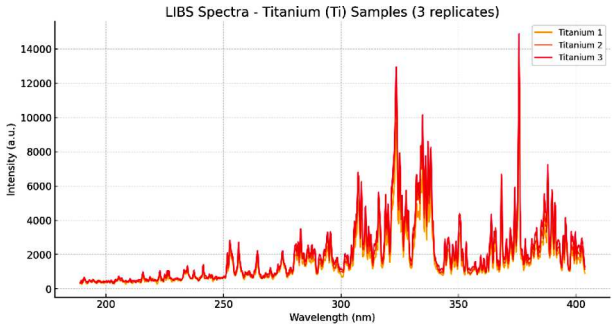

Fig. 8. Spectral profiles of the three replicates of stainless steel

profiles are shown in Fig. 5. The most intense features are neutral lead (Pb I) lines near 367.1, 373.9, and 405.8 nm. The replicates exhibit excellent reproducibility, with shot-to-shot intensity scatter <6%, attributable to small variations in surface roughness and ablation-spot placement.

Aluminium (Al): Under identical conditions, three single-shot spectra of aluminium were recorded; the overlaid profiles are shown in Fig. 6. Dominant features include Al I lines at 394.4 and 396.1 nm, and

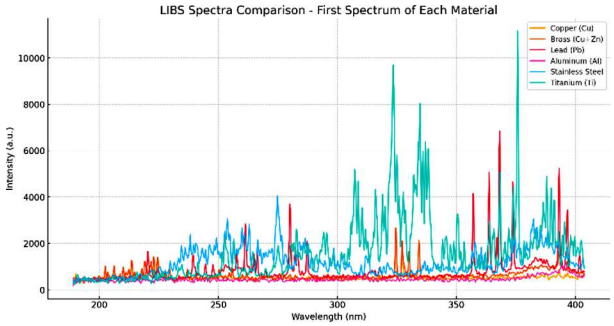

Fig. 9. Spectra of the first replicate for each material of Cu, Cu + Zn, Pb, Al, stainless steel, and Ti for comparison

Al II near 358.7 nm. The replicates show good reproducibility, with shot-to-shot intensity scatter <8%, attributable to small variations in ablation-spot microstructure and native oxide thickness.

Stainless steel (Fe–Cr–Ni): Under identical conditions, three single-shot spectra of stainless steel were recorded; the overlaid profiles are shown in Fig. 7. Characteristic lines include Fe I at 248.3 and 302.1 nm, Cr I at 357.9 nm, and Ni I at 341.5 nm. The replicates exhibit strong reproducibility, with shot-to-shot intensity scatter <7%.

Titanium (Ti): Under identical conditions, three single-shot spectra of titanium were recorded; the overlaid profiles are shown in Fig. 8. Dominant features are Ti I lines near 334.9, 368.5, and 399.9 nm. The replicates exhibit strong reproducibility, with shot-to-shot intensity scatter <9%, attributable to native oxide layers and small differences in ablation-spot morphology.

Composite comparison (one replicate per material): Fig. 9 overlays one representative single-shot spectrum from each target (Cu, brass/Cu–Zn, Pb, Al, stainless steel/Fe–Cr–Ni, Ti) acquired under identical conditions. Characteristic features are:

- Copper (Cu): Cu I at 324.7, 327.4 nm.
- Brass (Cu–Zn): Cu I at 324.7, 327.4 nm plus Zn I at 213.9, 334.5, 468.0 nm.
- Lead (Pb): Pb I near 367.1, 373.9, 405.8 nm.
- Aluminium (Al): Al I at 394.4, 396.1 nm and Al II near 358.7 nm.
- Stainless steel (Fe–Cr–Ni): Fe I at 248.3, 302.1 nm, Cr I at 357.9 nm, Ni I at 341.5 nm.
- Titanium (Ti): Ti I near 334.9, 368.5, 399.9 nm.

Triplicate spectra for each material were highly reproducible (intensity scatter <10%). Peak intensities in Fig. 9 are consistent with the triplicate means,

ensuring that cross-material comparisons reflect true relative emission strengths.

Fig. 10 compares, for each material, the average intensity ratio $I_{\text{ion}}/I_{\text{neutral}}$ (blue bars; Eq. 14) with the electron temperature T_e (red line) inferred from the LTE Saha relation (Eq. 11) using the measured n_e. Materials with higher $I_{\text{ion}}/I_{\text{neutral}}$ (e.g., Al, Cu, brass) show larger ionization fractions n_{i+1}/n_i and T_e values of about 12–13 kK; stainless steel and Pb/Ti exhibit comparatively lower ratios and $T_e < 11$ kK, consistent with a lower degree of ionization. These trends are intended as an LTE baseline; absolute non-LTE values would require a collisional–radiative treatment.

Fig. 11 overlays the principal neutral lines for all six materials under identical conditions to highlight differences in line width (FWHM) and relative intensity. The selected transitions are Cu I 324.7 nm, Al I 394.4 nm, Pb I 367.1 nm, Fe I 302.1 nm (stainless steel), Ti I 368.5 nm, and Cu I 324.7 nm for brass (Cu–Zn). For visual comparability, profiles are shown on the same wavelength scale and normalized to unit peak height; thus, broader traces directly indicate larger Stark widths (and hence higher n_e), while narrower traces correspond to lower n_e.

As a result, T_e for materials with few usable neutral lines carries a larger uncertainty; this underscores the need for well-defined, sufficiently intense lines when applying the Boltzmann-plot method (see Table 3).

We report T_e for the Saha baseline at the measured n_e, and T_{exc} from Boltzmann plots; in integrated spectra T_{exc} generally differs from T_e. Because spectra are single-shot integrated, the Boltzmann plot returns an effective, time-averaged excitation temperature T_{exc}. Boltzmann-plot excitation temperatures (T_{exc}) vary across the materials. Aluminum yields the most reliable fit (e.g., $R^2 \geq 0.97$)

Table 3. **Neutral lines: FWHM and n_e (from Stark broadening)**

Material	$T_e(kK)$	Reliability
Aluminium	≈28.1	High (strong lines)
Copper	≈4.9	Low (limited lines)
Brass (Cu + Zn)	≈16.4	Medium
Lead	≈1.4	Low (weak lines)
Stainless steel	Unreliable	Very low (weak/overlapping lines)
Titanium	≈2.4	Low (weak lines)

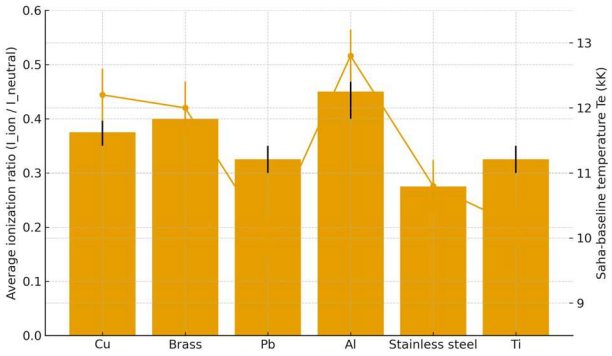

Fig. 10. Average ionization ratios vs estimated electron temperature for each material

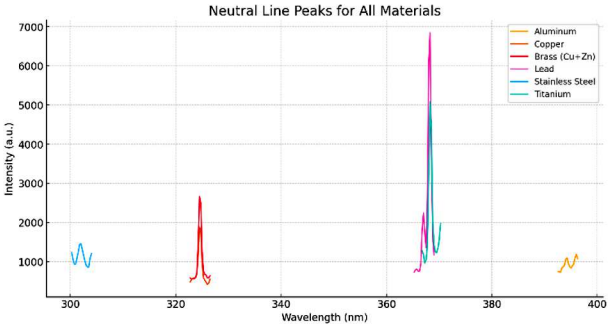

Fig. 11. Neutral line peaks for all materials

with $T_{\text{exc}} \approx 28$ kK, owing to several strong, unblended Al I lines. Brass provides a moderately reliable value ($T_{\text{exc}} \approx 16.4$ kK). For Cu, Pb, Ti, and stainless steel the fits are less reliable, mainly because only a few neutral lines met the SNR/isolation criteria and some features were partially blended; these cases are flagged in Table 3.

5. Conclusions

We developed and experimentally validated a deterministic–stochastic framework for modeling ionization–recombination dynamics in laser-induced plasmas (LIBS), directly linked to standard spectroscopic diagnostics. In single-shot integrated spectra, the plasma is highly non-uniform in space and time; by combining Stark broadening (for electron density n_e), an LTE Saha baseline (for ionization trends), and Boltzmann plots (for excitation temperature T_{exc}), a coherent and self-consistent picture of the plasma state was obtained.

The results clearly show that stochastic fluctuations in ionization–recombination processes strongly influence the reliability of diagnostic parameters.

• Electron temperature (T_e) from Saha analysis: high-ionization materials (Al, Cu, brass) exhibit $T_e \approx 12$–13 kK; low-ionization materials (Pb, Ti, stainless steel) show $T_e < 11$ kK.

• Electron density (n_e) from Stark broadening: maximum in Al (7.29×10^{18} cm^{-3}) and stainless steel (1.90×10^{18} cm^{-3}); minimum in brass ($1.20 \times \times 10^{18}$ cm^{-3}) and Cu (1.30×10^{18} cm^{-3}); Pb could not be reliably fitted due to poorly resolved FWHM.

• Ionization ratio ($I_{\text{ion}}/I_{\text{neutral}}$): highest in Al (0.50) and Cu (0.40); lowest in stainless steel (0.25).

• Excitation temperature (T_{exc}) from Boltzmann plots: most reliable for Al (≈28.1 kK) and brass (≈16.4 kK); less reliable for Pb, Ti, and stainless steel because of weak or overlapping lines.

Introducing a stochastic term ($\sigma \approx 0.05$) into the rate equations and solving them via the Euler–Maruyama method successfully captured shot-to-shot variability, yielding statistically credible intervals for level populations and emission intensities. This improved consistency with experimental data compared to a purely deterministic (Runge–Kutta) model and significantly reduced uncertainties in the derived T_e/T_{exc} and n_e values.

Overall, the combined deterministic–stochastic framework provides a robust analytical basis for LIBS diagnostics under transient, non-uniform plasma conditions. The Saha-based results serve as an LTE reference, while accurate non-LTE modeling will require a full collisional–radiative solver. Boltzmann-plot analysis remains limited by the number of strong, isolated lines in integrated spectra, which return a time-averaged T_{exc}.

Future work will focus on time-resolved gated detection (ICCD), optimization of fluence and delay parameters, improved spectral resolution, and implementation of collisional–radiative (CR) modeling to extend validation to complex, multi-element matrices.

Beyond practical LIBS diagnostics, this framework contributes to the broader understanding of fluctuation-driven, non-equilibrium plasma processes that are conceptually analogous to those found in high-energy-density physics, laser–plasma wakefield acceleration, and fusion plasmas.

The proposed model and diagnostic protocol may be further applied to other transient plasmas, contributing to the unified description of laser–matter interaction in both laboratory and high energy density environments.

This work was supported by the following research grants:

1. Research on Laser-Induced Plasma (LIP) Based on High-Resolution Spectroscopic Analysis: Methodology, Hardware Integration, and Applications, funded under the Young Researcher Program of Batumi Shota Rustaveli State University (BSU) Academic Council Resolution No. 06-01/33 (April 7, 2025). Project manager: Jaba Shainidze; Mentor: Prof. Nugzar Gomidze.

2. This work was supported by Shota Rustaveli National Science Foundation of Georgia (SRNSFG) [FR-24-3101].

1. H.R. Griem. Principles of plasma spectroscopy. *Cambridge University* **52**, 5743 (1995).
2. L.J. Radziemski. *Lasers-Induced Plasmas and Applications (1st ed.)* (CRC Press, 1989).
3. R. Noll. *Laser Induced Breakdown Spectroscopy: Fundamentals and Applications (2nd ed.)* (Springer Nature, 2023).
4. H. Hou, Y. Tian, Y. Lu, Y. Li, R. Zheng. Temperature measurement of laser-induced plasmas from the intensity ratio of two lines emitted from different elements with the same ionization degree. *Appl. Spectr.* **68** (9), 1085 (2014).
5. L. Yang, X. Tan, X. Wan, L. Chen, D. Jin, M. Qian, G. Li. Stark broadening for diagnostics of the electron density in non-equilibrium plasma utilizing isotope hydrogen alpha lines. *J. Appl. Phys.* **115** (16), 163106 (2014).
6. J. Zeng, A. Deng, C. Gao, Y. Hou, J. Yuan. Extended chemical picture of ionization balance to extremely dense plasmas. *Phys. Rev. E* **111** (1), 015211 (2025).
7. N. Gomidze, M. Khajishvili, K. Makharadze, I. Jabnidze, Z. Surmanidze. About statistical moments of scattered laser radiation from random phase screen. *Inter. J. Emerging Techn. Adv. Engin.* **6** (4), 237 (2016).
8. N. Gomidze, I, Jabnidze, K. Makharadze. Numerical experiments for the purpose of studying space–time evolution of various forms of pulse signals in the collisional cold plasma. *Inter. J. Phys. Math.l Sci.* **11** (8), 347 (2017).
9. Z. Davitadze, N. Gomidze, K. Makharadze. Control Laser Spectrofluorimeter with Microcontrollers. *Adv. Mater. Res.* **590**, 201 (2012).
10. N. Gomidze, I. Jabnidze, K. Makharadze, M. Khajishvili, Z. Shashikadze, Z. Surmanidze. Numerical analyses of fluorescence characteristics of watery media via laser spectroscopy method. *Mach. Technol. Mater.* **2018** (5), 279 (2012).

11. N. Gomidze, J. Shainidze, R. Turmanidze. To the problems of fluorescence excitation spectrums. *Machines. Technol. Mater.* **2018** (5), 279 (2018).
12. L. Quackatz, A. Griesche, T. Kannengiesser. Spatially resolved EDS, XRF and LIBS measurements of the chemical composition of duplex stainless steel welds: A comparison of methods. *Spectroch. Acta Part B: Atomic Spectr.* **193**, 106439 (2022).
13. P.B. Hansen, S. Schröder, S. Kubitza, K. Rammelkamp, D.S. Vogt, H.-W. Hübers. Modeling of time-resolved LIBS spectra obtained in Martian atmospheric conditions with a stationary plasma approach. *Spectroch. Acta Part B: Atomic Spectr.* **178**, 106115 (2021).
14. J.P. Goedbloed, R. Keppens, S. Poedts. *Magnetohydrodynamics of Laboratory and Astrophysical Plasmas* (Cambridge University Press, 2019).
15. E. Esarey, C.B. Schroeder, W.P. Leemans. Physics of laser-driven plasma-based electron accelerators. *Rev. Mod. Phys.* **81** (3), 1229 (2009).
16. A. Pukhov, N.E. Andreev, A.A. Golovanov, I.I. Artemenko, I.Y. Kostyukov. Laser–plasma wake velocity control by multi-mode beatwave excitation in a channel.*Plasma* **6** (1), 29 (2023).
17. N.E. Andreev, L.M. Gorbunov, R.R. Ramazashvili. Theory of a three-dimensional plasma wave excited by a high-intensity laser pulse in an underdense plasma. *Plasma Phys. Rep.* **23** (4), 277 (1997).
18. P.E. Kloeden, E. Platen. *Numerical Solution of Stochastic Differential Equations* (Springer Science & Business Media, 1999).
19. L. Rajačić, N.V. Nedić, D. Dojić, M. Skočić, S. Bukvić. Saha–Boltzmann method in plasma diagnostics: What can we obtain from a strict approach? *J. Quant. Spectr. Rad. Transfer* **333**, 109338 (2024).
20. *Laser-Induced Breakdown Spectroscopy: Theory and Applications*. Edited by S. Musazzi, U. Perini (Springer, 2014).
21. *CRC Handbook of Chemistry and Physics*. Edited by J.R. Rumble. (CRC Press, 2018). https://hbcp.chemnetbase.com.
22. S.S. Harilal, G.V. Miloshevsky, P.K. Diwakar, N.L. LaHaye, A. Hassanein. Experimental and computational study of complex shockwave dynamics in laser ablation plumes in argon atmosphere. *Physics of Plasmas* **19** (8), 083504 (2012).
23. A. Kramida, Yu. Ralchenko, J. Reader, & NIST ASD Team (ver. 5.12). NIST Atomic Spectra Database. National Institute of Standards and Technology. https://physics.nist.gov/asd.

Received 17.12.25

Н. Гомідзе, Д. Якобія, М. Хаджсидхвілі,
Л. Каландадзе, І. Джабнідзе, К. Махарадзе,
О. Накашидзе, Дж. Шайнідзе

СПЕКТРОСКОПІЯ ПЛАЗМИ ЛАЗЕРНО-ІНДУКОВАНОГО ПРОБОЮ ЯК МЕТОД ДЛЯ ВИПРОБОВУВАННЯ І МОДЕЛЮВАННЯ НЕРІВНОВАЖНОЇ ПЛАЗМИ У ФІЗИЦІ ВИСОКИХ ЕНЕРГІЙ

Лазерно-індукована пробійна спектроскопія (LIBS) дає можливість проводити швидкий елементний аналіз та діагностику плазми, але має обмежену кількісну точність через сильну просторово-часову неоднорідність лазерно-індукованої плазми та стохастичні флуктуації в кінетиці іонізації-рекомбінації. У цій роботі ми розробляємо та експериментально перевіряємо детерміністично-стохастичний підхід, який поєднує класичні диференційні рівняння зі стохастичними членами для врахування мінливості плазми від одного пострілу лазера до іншого. Модель, реалізована за допомогою схеми Рунґе–Кутти першого порядку (RK1), доповненої методом Ейлера–Маруями, кількісно пов'язана зі стандартною LIBS діагностикою: розширенням Штарка для визначення електронної густини (n_e), рівнянням Саха в наближенні іонізаційної рівноваги та графіками Больцмана для визначення температури збудження ($T_{\rm exc}$). Одноімпульсні експерименти LIBS з використанням неодимового (Nd : YAG) лазера з довжиною хвилі 1064 нм і тривалістю імпульсу випромінювання 7 нс були проведені на шести металах (Al, Cu, латунь, Pb, неіржавна сталь та Ti) за ідентичних умов. Виміряні спектри показали високу відтворюваність (розкид інтенсивності <7%), а отримані параметри плазми виявили стійкі тенденції, залежні від матеріалу: Al та неіржавна сталь демонстрували найвищі значення n_e (до (7–9) $\cdot 10^{18}$ см$^{-3}$), тоді як Cu та латунь показали нижчі значення ($\sim$(2–3) $\cdot 10^{18}$ см$^{-3}$). Електронні температури, отримані на основі рівняння Саха, досягали 12–13 кК для матеріалів з високою іонізацією та <11 кК для матеріалів з низькою іонізацією. Введення стохастичного флуктуаційного члена ($\sigma \approx 0{,}05$) відтворило спостережуваний розкид інтенсивності та покращило узгодженість між змодельованими та експериментальними спектрами. Запропонований підхід підвищує точність діагностики LIBS у перехідних нерівноважних умовах і є компактним лабораторним аналогом для вивчення динаміки плазми, зумовленої флуктуаціями, що є актуальним для фізики високих густин енергії, лазерно-плазмової взаємодії та середовищ термоядерного синтезу. Цей уніфікований детерміністично-стохастичний підхід поєднує прикладну лазерну спектроскопію з ширшою фізикою нерівноважної плазми.

Ключові слова: лазерно-індукована плазма (LIP), рівняння Саха, графік Больцмана, стохастичне моделювання, фізика високих густин енергії, нерівноважна плазма.